"Beware of Doping: Ta_2O_5 Nanotube Photocatalyst using CNTs as Hard Templates"

in *ACS Applied Energy Materials* **2018** 1 (3), 1256-1267,

To access the final edited and published work see https://pubs.acs.org/doi/abs/10.1021/acsaem.8b00006.

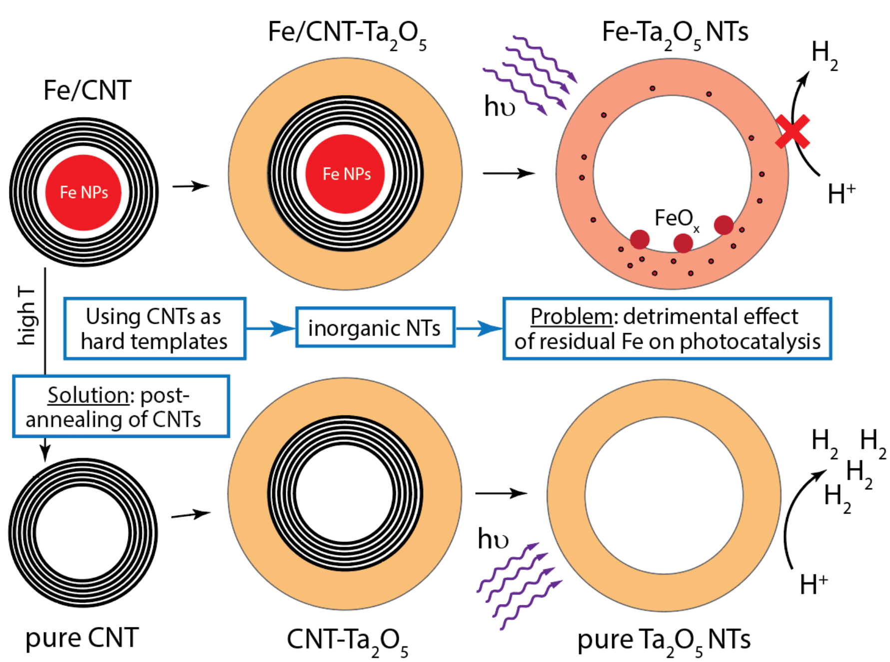

Beware of Doping: Ta_2O_5 Nanotube Photocatalyst using CNTs as Hard Templates

Alexey Cherevan,[a] Paul Gebhardt,[b] Andreas Kunzmann,[c] Rubén D. Costa,[d] and Dominik Eder[a]**

[a] *Institut für Materialchemie, Technische Universität Wien, Getreidemarkt 9, 1060, Vienna, Austria*

[b] *Fraunhofer-Institut für Solare Energiesysteme ISE, Heidenhofstraße 2, 79110, Freiburg, Germany*

[c] *Department Chemie und Pharmazie, Friedrich-Alexander Universität Erlangen-Nürnberg, Nikolaus-Fiebiger-Straße 10, 91058, Erlangen, Germany*

[d] *IMDEA Materials Institute, Eric Kandel 2, 28906 Getafe, Madrid, Spain*

alexey.cherevan@tuwien.ac.at and dominik.eder@tuwien.ac.at

Abstract

Nanostructuring constitutes a promising strategy to increase efficiency and stability of contemporary photocatalysts. Here we report on the synthesis of highly crystalline Ta_2O_5 nanotubes (NTs) by using carbon nanotubes (CNTs) as sacrificial hard templates and elucidate the role of residual Fe nanoparticles – often used as catalyst for the CNT growth – on their photocatalytic performance towards H_2 evolution. We show that when using as grown CNTs, the resulting Ta_2O_5 NTs contained detectable amounts of Fe and possessed negligible photocatalytic activity. When CNTs were, however, purified from Fe by thermally annealing the CNTs at 2100°C, the same synthetic procedure yielded pure Ta_2O_5 NTs that showed a 40-fold increase in activity compared to the Fe-containing counterpart. A complementary set of analytical techniques in a combination with additional model experiments indicate that the detrimental effect of the residual Fe on the photocatalytic activity originate from atomic doping and formation of a segregated FeO_x phase within the Ta_2O_5 matrix that can both act as efficient electron traps. Our result highlights that the presence of residual catalyst needs to be taken into account when using CNTs as hard templates and generally illustrates a possible effect of unintentional dopants that are often not considered in preparing functional nanostructures.

Keywords: *sol-gel, carbon nanotubes, CVD, photocatalysis, electron trapping, metal doping, thermal annealing*

Introduction

Last decades have been a witness of a rapid growth and evolution of photocatalysis – a valuable research field that provides access to a number of unique redox chemistries by means of light-assisted catalysis.[1–5] Photocatalytic processes include waste water treatment and air purification, selective oxidation and reduction reactions, CO_2 valorization, and water splitting.

Despite significant progress in this research field, contemporary photocatalysts still suffer from three main shortcomings, namely (i) insufficient light absorption in the visible range that limits the number of utilized photons from sunlight, (ii) extensive electron-hole recombination that reduces charge carrier lifetimes, and (iii) poor catalytic properties of bare photocatalyst surfaces that often require noble metal co-catalyst deposition.

A number of techniques have been implemented in order to improve properties of bulk oxide photocatalysts, addressing the aforementioned shortcomings. As such, extensive attention has been paid to the fabrication of different one-dimensional (1D) nanostructures: nanowires, nanorods, nanotubes (NTs), and nanofibres.[6] Compared to 3D materials, these nanostructures provide not only a high surface area available for the catalytic process, but also have shorter diffusion lengths of photoexcited carriers towards the solid-liquid interface.[7–10] Additionally, the carriers are free to move throughout the length of such nanostructures, which has been shown to reduce the probability of electron-hole recombination.[11]

Inorganic NTs can be prepared by means of sol-gel,[12,13] hydrothermal,[14,15] and electrochemistry[16–19] methods. Among them, anodization is best suited to prepare high quality inorganic photo-electrodes. However, the method has apparent limitations when large quantities of free-standing powders are desired. Another approach that can be used to produce NT structures is the use of carbon nanotubes (CNTs) as nanosized tubular templates, which can be removed after a desired inorganic component is deposited.[20,21] This flexible approach has already been realized to nanostructure a variety of functional oxides yielding examples of TiO_2,[22] ZrO_2,[23] Al_2O_3,[24] In_2O_3,[25] NiO,[26] $Pb(Zr_{0.52}Ti_{0.48})O_3$,[27] Fe_2O_3,[28] Cr_2O_3[29] and Co_3O_4[30] NTs, however, little attention has so far been paid to the quality of the CNT template used for the synthesis.

Chemical vapor deposition (CVD) is the most widely used way to prepare large batches of CNTs.[31] However, CVD often requires the use of catalytic particles that are either predeposited on a substrate or formed *in situ* from low vapor pressure precursors during the CNT growth. Such catalysts are mostly single metals (Fe, Co, Ni, Mo, Au) or metal alloys (FeCo, FeMo, NiMo, FeCu) that eventually reside inside the as-grown CNTs.[32,33]

With regard to that, only a few works, in which CNTs were produced *via* CVD, have discussed the influence of the residual catalyst on the final morphology, composition and, if applicable, photocatalytic performance of the functional NTs.[34] Several literature reports have actually used such residual metal catalyst-containing CNTs to prepare TiO_2 NTs with controlled levels of Fe doping.[35,34] The authors reported increased photocatalytic activities of the Fe-doped-TiO_2 NTs with regard to P25 TiO_2 reference nanoparticles, but have not compared the performance to Fe-free-TiO_2 NTs of similar morphology. However, residual catalyst may often account for up to 10 wt. % of the nanocarbon mass fraction and can therefore strongly interact (e.g. dope, alloy, modify, create additional solid-solid interfaces) with the inorganic layer upon high temperature CNT oxidation, thus affecting a number of the product's functional properties.

To address this knowledge gap, we produced and investigated Fe-containing-Ta_2O_5 NTs that we fabricated *in situ* by using residual Fe-catalyst-containing CNTs as sacrificial hard templates. We show that Fe can dope and form a segregated FeO_x phase in the produced Ta_2O_5 NTs and both species negatively affect the photocatalytic performance by acting as efficient electron traps. We demonstrate that the photocatalytic activity can be boosted by using Fe-free (pre-purified) CNTs as template, therefore resulting in pure Ta_2O_5 NTs exhibiting strongly increased H_2 evolution rates with photonic efficiencies of up to 0.8 %. Our work provides a general guidance on using CNT templates with residual catalysts as a means of controllable doping, highlighting that the presence of residual catalyst in CNTs needs to be taken with caution when preparing functional nanostructures for energy applications.

Results

We synthesized CNTs *via* a standard, widely-used CVD protocol using ferrocene as a source for the Fe catalyst (see Methods for experimental details). The as-grown CNTs were hundreds of microns long, with the average diameter of 80 nm and, as revealed by TEM and TGA, contained around 3.5 wt. % of residual iron particles mainly incorporated in the inner tube channels (Supporting **Figure S1a** and **d**). The CNTs were post-annealed in argon at 1000 °C (CNT1000) to remove the amorphous carbon and render the surface more graphitic, while leaving the Fe NPs intact (Supporting **Figure S1b**).

To prepare 1D inorganic NTs, we followed a recently described two-step synthetic protocol that is illustrated in **Scheme 1**.[36] In order to allow homogeneous attachment of metalorganic precursor, the CNT1000 were non-covalently functionalized with benzyl alcohol[37] and consequently coated with a thin and uniform Ta_2O_5 layer *via* a solvothermal sol-gel process yielding CNT-Ta_2O_5 hybrid material[38] (**Figure 1a** and Supporting **Figure S2** and **S3**). In a second step, we removed the carbon template and simultaneously crystallized the oxide layer *via* a heat treatment in ambient air at elevated temperatures (780 °C). During the latter step, Fe nanoparticles get released from the carbon matrix, get oxidized and mobilized and come into contact with the Ta_2O_5 layer promoting interaction between the compounds that eventually results in the incorporation of iron species.[39]

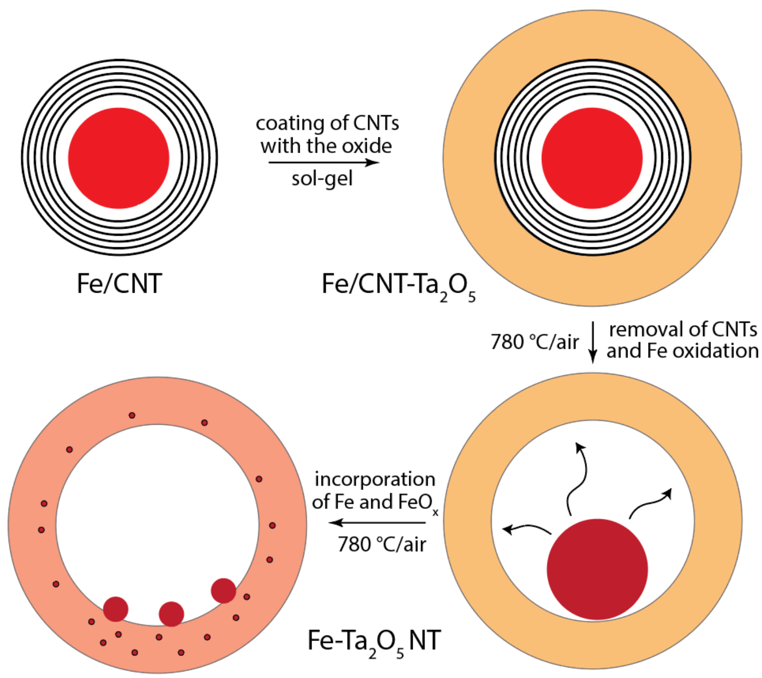

Scheme 1. Process of the Ta_2O_5 NT synthesis: first, CNTs are coated with the Ta_2O_5 layer; second, the resulting hybrid is thermally treated in air to remove the nanocarbon template and release the Fe NPs leading to Fe incorporation.

As revealed by transmission electron microscopy (TEM in **Figure 1b**), this procedure indeed yieled the desired 1D structures with the tubular morphology resembling that of the CNT templates, while also appearing to be highly crystalline (**Figure 1b**, inset). Overview scanning electron microscopy (SEM) images in **Figure 1c** also show homogeneity of the samples. As a side note, depending on the initial thickness of the Ta_2O_5 layer deposited on the CNTs, we could obtain two types (complete and incomplete) of the Ta_2O_5 NT structures (see Supporting **Figure S2** and **S3**). This observation is in line with our previous report where we have shown that the CNT template may have a strong influence on the crystallisation of the inorganic coating.[40] Since both types behave similarly with regard to the Fe incorporation, further discussion will only consider complete Ta_2O_5 NTs shown in **Figure 1**.

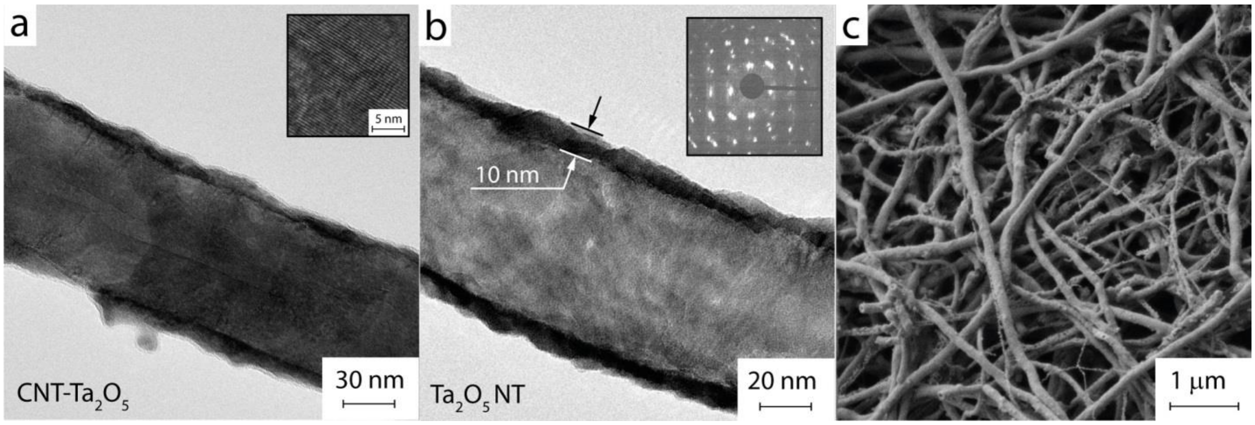

Figure 1. Representative TEM (a, b) and SEM (c) images of the CNT-Ta_2O_5 hybrid (a) and resulting Ta_2O_5 NTs (b, c). Inset in (a) shows single crystalline nature of the oxide coating; inset in (b) shows electron diffraction pattern of the full area.

Purification of the CNTs from the residual Fe catalyst particles requires more targeted post-treatments[41] and to ensure complete removal of Fe from the inner channels, the as-grown CNTs were annealed in argon at 2100 °C for 6 h (CNT2100). TGA data (Supporting **Figure S1d**) show a strong decrease in the amount of Fe residues while TEM investigations also confirm the absence of embedded Fe particles (Supporting **Figure S1c**) after the high-temperature annealing. Raman spectroscopy (Supporting **Figure S1e**) of both CNT samples (CNT1000 and CNT2100) further reveal that no strong differences in the surface chemistry and crystallinity were introduced by the different post-annealing procedures. The CNT2100 sample was subsequently used to synthesize Fe-free-Ta_2O_5 NTs following an identical protocol as was used for the CNT1000 sample.

As the result of using CNT templates with similar surface, crystallinity and morphology, both Ta_2O_5 NT samples reveal similar morphology and crystallinity of the oxide layer after the template removal. As such, X-ray diffraction (XRD) in **Figure 2** revealed very similar diffraction patterns for Fe-free and Fe-containing Ta_2O_5 samples. Peak deconvolution confirms the presence of expected β-Ta_2O_5 phase in both cases with a little content of superstructure similar to the one described by Audier *et al.*[42,43] Further detailed peak comparison (Supporting **Figure S4**) indicates small differences in peak intensity and position between the two samples, yet no clear trend in peak shifts can be revealed. This is further confirmed by the Rietveld refinement shown in **Figure 2b** which indicates that a, b, c and volume of the basic β-Ta_2O_5 cell are nearly unaffected by the presence of Fe impurities. Importantly, the crystalline phase of the Fe impurities in the Fe-Ta_2O_5 sample cannot be reliably identified by XRD most likely due to its insufficient amount.

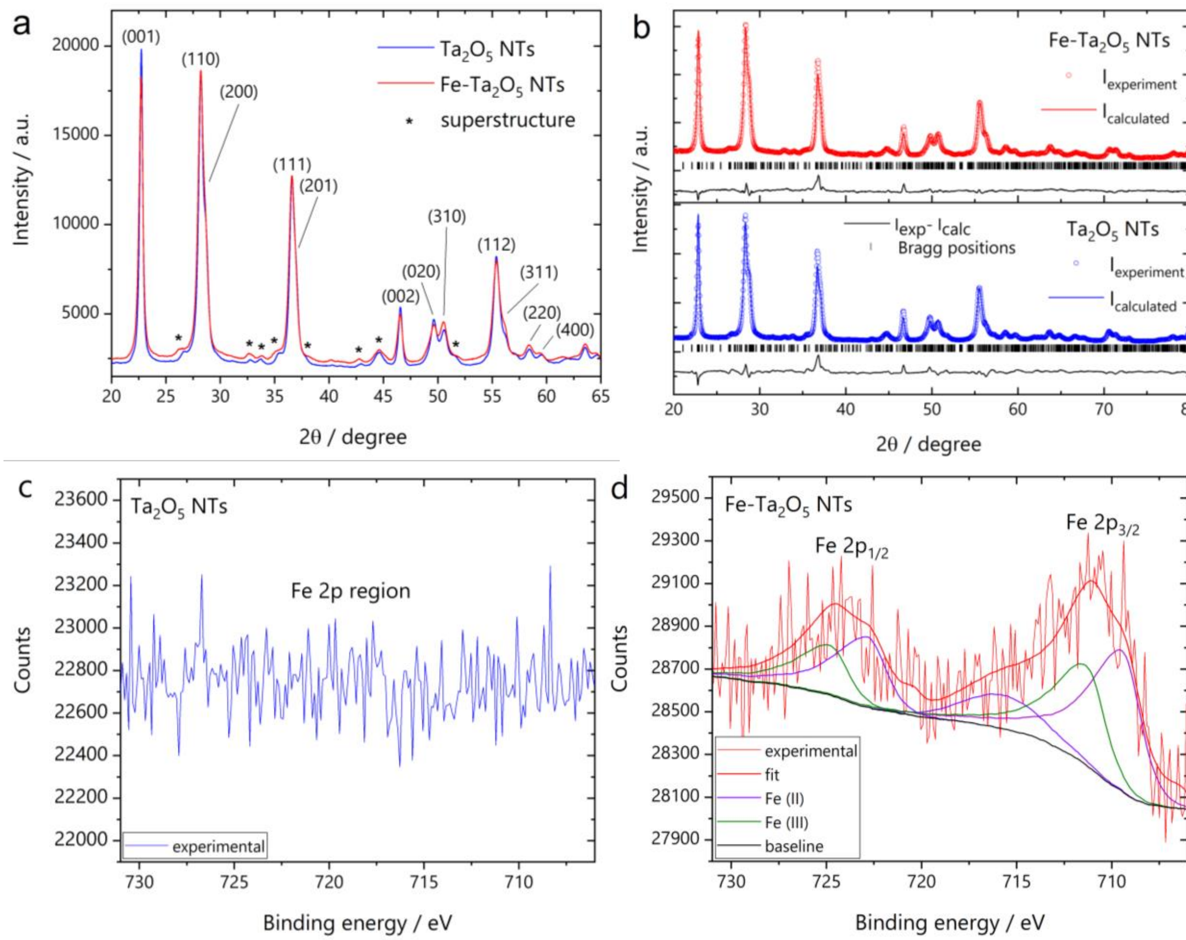

Figure 2. XRD patterns of the Fe-free and Fe-containing Ta_2O_5 NTs indicating similar crystalline phase content in both samples (a) and the corresponding refinement fits (b) as well as XPS spectra (Fe 2p region) of the samples that confirm the absence of iron impurities in the Ta_2O_5 NTs (c) and the presence of both Fe^{2+} and Fe^{+3} in the Fe-Ta_2O_5 NTs (d).

The crystalline nature of the NT structures was further confirmed by high-resolution TEM (HRTEM) studies. Images of both samples (example in **Figure 1b**) reveal that the NT walls (around 10 nm in thickness) are single crystalline throughout their thickness. In addition, they are composed of extended crystalline domains as confirmed by electron diffraction (ED) pattern shown in the inset. We further estimated the average crystallite size of Ta_2O_5 grains in both samples from XRD data using the Scherrer equation.[44] The calculation yields values of 16.7 and 14.8 nm for the Ta_2O_5 and Fe-Ta_2O_5 sample, respectively, indicating that the Fe incorporation introduced a minor loss in the crystallinity of the Ta_2O_5 matrix.

According to the TEM- and SEM-based energy dispersive X-ray spectroscopy (EDX) maps shown in **Figure 3** (additional data in Supporting **Figure S5**) both materials are composed of Ta and O matrix species, while the Fe-Ta_2O_5 NT sample also contains a weak, but distinguishable and evenly-distributed Fe signal. The maps also indicate some areas having locally higher Fe concentration, possibly related to areas close to those where Fe NPs were initially trapped. Unfortunately, EDX does not provide sufficient spatial resolution to distinguish between types of incorporated Fe.

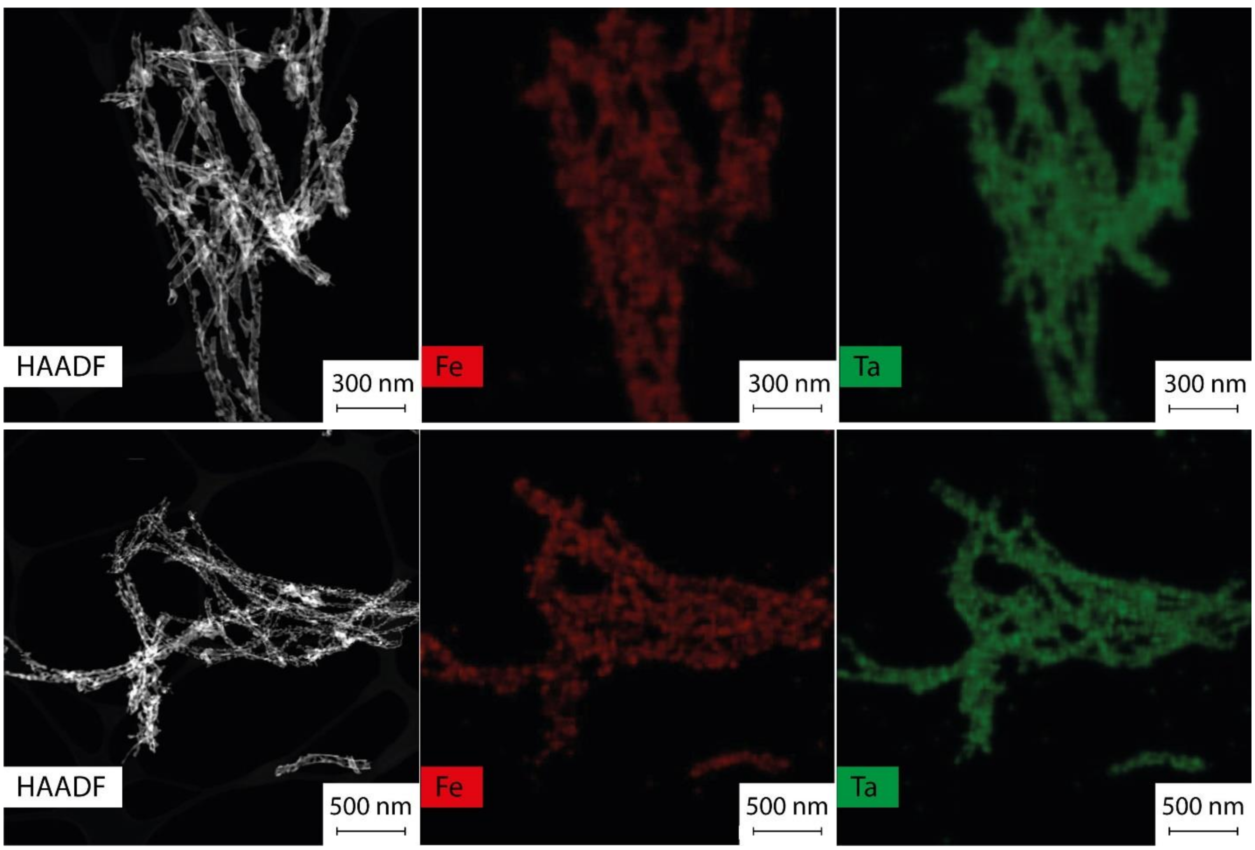

Figure 3. High-angle annular dark field (HAADF) images and EDX maps of the Fe-containing Ta_2O_5 NTs indicating homogeneous distributing of Fe signal in the NT matrix.

To reveal the oxidation state of the Fe impurities, we performed X-ray photoelectron spectroscopy (XPS) analyses. The spectra of the Ta 4p region in Supporting **Figure S6** confirm that Ta is present in both materials in its most stable +V oxidation state. XPS of the Fe-Ta_2O_5 NT sample additionally reveals 1.2 at. % of Fe that is present in the technique-sensitive surface layer (**Figure 2d**), in line with values obtained from TGA (see

Supporting **Figure S1**). Further peak analysis indicates existence of both Fe^{2+} and Fe^{3+} in the Fe-containing NTs with atomic ratio of 1.8:1, respectively. No presence of metallic Fe could be identified.

XPS data allows us to assume that 54% of Fe atoms is present in the form of Fe_3O_4 (includes all Fe^{+3} species) which is the thermodynamically most stable form;[39] while the rest 46% of the iron is present in the form of Fe^{2+} species that might be additionally incorporated as atomic dopants in the Ta_2O_5 matrix. This assumption, however, is rather counterintuitive if one considers the ionic radius of Ta^{5+} and Fe^{2+} with the coordination number of 6 to be 0.64 Å and 0.75 Å, respectively.

Raman spectroscopy provides additional insights into the defect and impurity structure of the Ta_2O_5 NT samples. The spectrum of the pure Ta_2O_5 NTs in **Figure 4a** contains 7 main peaks that can be assigned to various vibrational modes of the oxide structure.[45] In contrast, the spectrum of Fe-Ta_2O_5 NTs in **Figure 4b** contains fewer peaks – *e.g.*, peaks at *ca*. 360 and 490 and 710 cm^{-1} that correspond to deformation and stretching O-2Ta and O-3Ta modes in TaO_6 octahedra are completely vanished – that also get broader indicating that the structure of Fe-Ta_2O_5 NTs is more disordered and may incorporate additional defects.[46] This observation is in line with the decreased crystallite size of the latter sample derived from XRD data and can further evidence the presence of Fe doping.

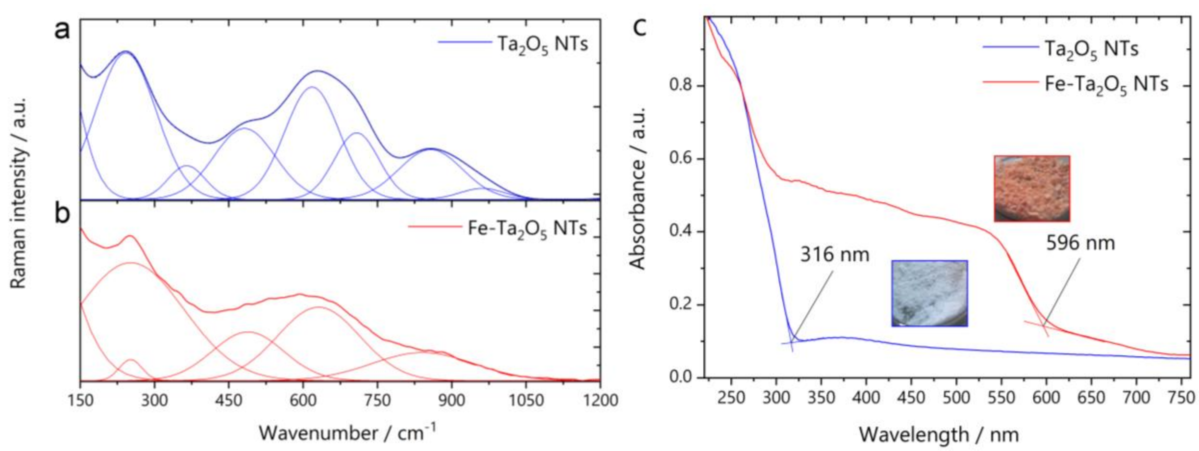

Figure 4. Raman spectra of (a) Fe-free and (b) the Fe-containing Ta_2O_5 NTs as well as (c) the digital photographs of the powders and their UV-vis absorption spectra.

The Fe incorporation is clearly noticed by the change in the sample color (**Figure 4c**, insets). This is confirmed by diffuse-reflectance spectroscopy (DRS) measurements used to quantify light absorption properties of both samples in solid-state. Spectrum of the

Ta_2O_5 NTs shown in **Figure 4c** is in line with the expected optical band gap value of the oxide (3.9 eV) reported earlier.[45] DRS of the Fe-containing Ta_2O_5 NTs additionally reveals extended absorption in the visible light range spanning well beyond 600 nm. It also features a clear absorption edge at ca. 600 nm (2.07 eV) that may correspond to the presence of earlier proposed Fe_3O_4 phase,[47] however, other iron oxides cannot be reliably excluded. Additional absorption above 600 nm can be attributed to the presence of new interband states in Ta_2O_5 forbidden zone as a result of atomic doping by Fe ions.[48]

The overall characterization data suggest that we have successfully designed two Ta_2O_5 NTs samples with comparable morphology, composition, structure and dimensions, yet one of them incorporated the residual Fe in two forms: doping and segregated FeO_x phases. Now, in order to unravel the effect of Fe incorporation, we investigated photocatalytic performance of the Fe-Ta_2O_5 NTs and Ta_2O_5 NTs.

Photocatalytic performance

Both materials were tested towards H_2 evolution from sacrificial water splitting under UV-vis illumination (see Methods for experimental details). Reaction profiles (rates of H_2 production) are shown in **Figure 5a** along with the baseline which corresponds to the blank experiment performed without any photocatalyst present in the reaction medium. The photocatalytic activity of the Fe-Ta_2O_5 NTs powder suspensions, calculated from steady-state H_2 evolution rate, was found to be rather low with photonic efficiency (see calculations in Supporting information) of as much as just 0.05 %, despite its extended absorption in the visible light range. Additionally, this value is much lower than that of similar materials reported in literature and that of a bulk Ta_2O_5. Interestingly, despite the weaker light adsorption, the pure Ta_2O_5 NTs demonstrated a 40-fold increase in activity (photonic efficiency of 0.8 %) with respect to the Fe-containing counterpart (details in Methods). This finding contradicts a number of literature reports where it has been shown that introduction of foreign cations (e.g. Fe) into a photocatalyst structure (e.g. Ta_2O_5) results in improved photocatalytic performance.[49–51]

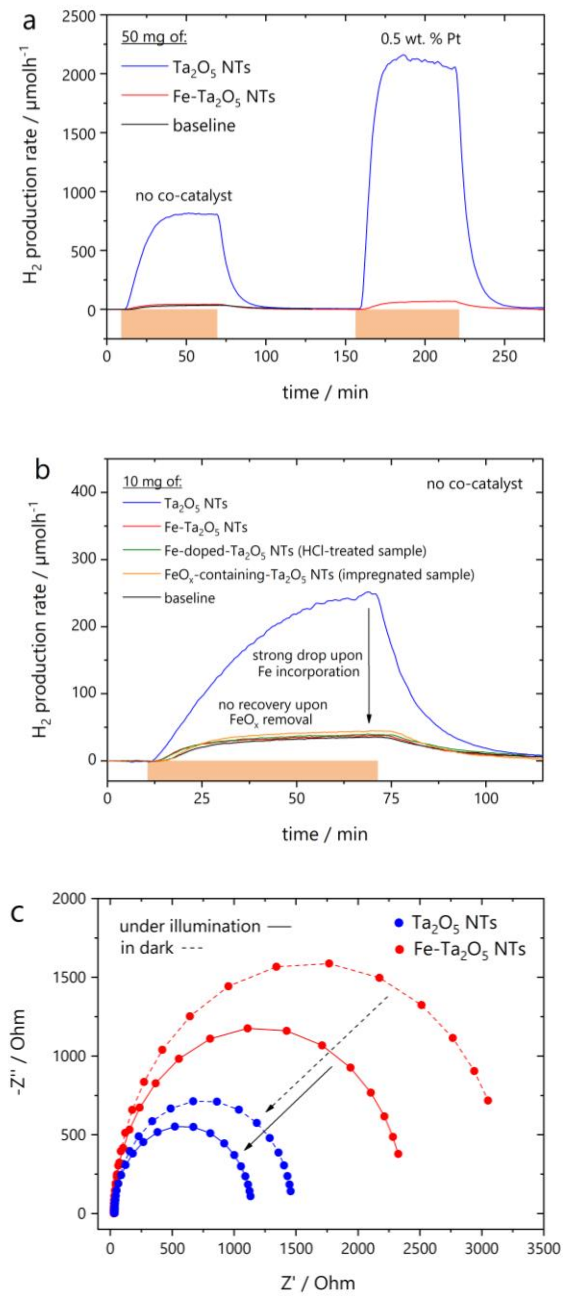

Figure 5. (a) Photocatalytic hydrogen evolution tests of the Fe-free and the Fe-containing Ta_2O_5 NTs with and without the presence of Pt co-catalyst performed with 50 mg powders, and (b) additional tests with HCl-treated and impregnated samples without any Pt present performed with 10 mg powders. Colored areas represent time periods of light illumination. The graph also contains the baseline which corresponds to the black experiment performed without any photocatalyst present. The H_2 evolution in this case is the result of photo-assisted MeOH oxidation (photo-reforming) and the rate is subtracted from photocatalytic activities of the rest of the samples when their performance is compared and discussed in the main text. (c) Direct comparison of the electrochemical impedance spectroscopy (EIS) spectra of Ta_2O_5 and Fe-Ta_2O_5 NTs at a bias voltage of -0.6 V under illumination (solid lines) and dark conditions (dashed lines), respectively.

Discussion

A closer inspection of current literature suggests that the effect of doping on the photocatalytic performance is a trade-off between improved light absorption capability and increased electron-hole trapping recombination, while both rise with higher amount of incorporation.[52] We know that the amount of Fe incorporation obtained by using standard CVD-grown CNTs as a template to prepare such 1D NTs lies in the range between 1 and 5 wt. % (TGA in Supporting **Figure S1d**), that is far higher than the optimal doping value reported elsewhere.[53] Moreover, in our case – as derived from XPS, EDX and Raman data – the Fe incorporation is likely to result not only in pure doping, but also in the formation of segregated Fe oxide phase, which we believe can also act as an electron acceptor[54] thus also diminishing photocatalytic performance – see **Scheme 2**.

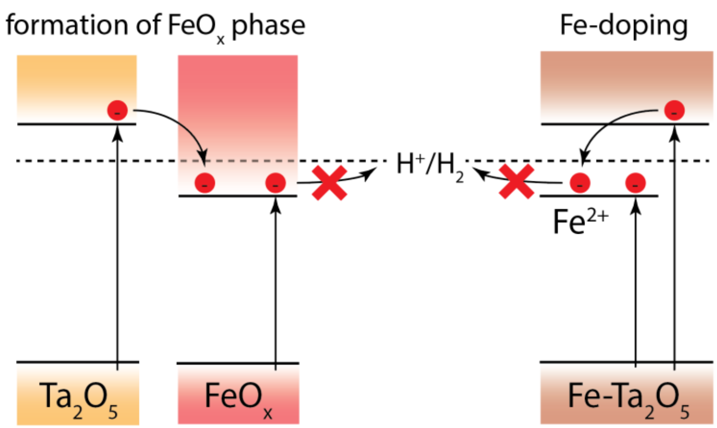

Scheme 2. Schematic representation of the energy band structure of the resulting Fe-Ta_2O_5 NTs in the case of atomic Fe doping (right) and formation of segregated FeO_x NPs (left) that in both cases can act as electron traps and diminish photocatalytic performance towards hydrogen evolution reaction.

To verify our hypothesis and further evaluate the effect of the Fe doping and the presence of FeO_x impurities we have performed additional experiments with model samples. First, we have selectively removed FeO_x from the Fe-containing Ta_2O_5 NTs by treating the powdered sample with 5 M HCl (see Methods). Acid treatment is known to dissolve segregated Fe oxides, while leaving the atomically-doped Fe intact. Interestingly, the resulting Fe-doped-Ta_2O_5 NTs did not lose their reddish color, indicating that main optical absorption edge at 600 nm can exclusively be associated with the presence of atomic doping. Photocatalytic experiments shown in **Figure 5b** reveal that the HCl-treated sample also exhibits a negligible activity similar to the one recorded for the sample before the treatment. This result indicates that Fe-doping is one of the factors for the observed detrimental effect. To further elucidate the role of FeO_x impurities, we impregnated our pure Ta_2O_5 NT sample with a corresponding amount of $Fe(NO_3)_3$ following by the heat treatment at 250 °C (see Methods). Using ferrous nitrate with its low decomposition temperature allowed us to prepare FeO_x-containing Ta_2O_5 sample, while avoiding possible Fe doping.[55] Photocatalytic H_2 evolution tests shown in **Figure 5b** revealed a strong loss in activity after the impregnation thus indicating that also incorporation of FeO_x impurities alone is detrimental for the performance of the Ta_2O_5 NTs.

To further elucidate the underlying reasons for the decreased photocatalytic performance of the Ta_2O_5 NTs upon Fe incorporation, we additionally performed electrochemical impedance spectroscopy (EIS) on Fe-free and Fe-containing Ta_2O_5 NT powders that were deposited on transparent conductive electrodes in the form of thin films (see Methods). The EIS measurements were carried out in dark and under illumination at different applied voltages using a symmetric cell and a reactive redox electrolyte to evaluate the effect of Fe on the charge carrier dynamics.

Figure 5c and Supporting **Figure S9** display the Nyquist plots whose width is related the charge transfer resistance at the electrode/electrolyte interface R_k and charge transport resistance R_w under dark and illumination conditions, respectively. In the dark, Fe-Ta_2O_5 cells show larger semicircles than those of Ta_2O_5 films. This indicates a diminished interfacial electron recombination R_k at the electrode/electrolyte interface, suggesting that the presence of Fe impurities induces intra band gap states that act as electron traps. In contrast, upon illumination the semicircles get significantly reduced, indicating a considerable density of excited carriers in the samples. Here, independently of the applied bias the Fe-Ta_2O_5 films show at least two times larger R_w values than the Ta_2O_5 films, pointing to a worse charge transport of the former sample. This is further supported by the higher capacitance C_w and charge collection efficiency η_{coll} of the Ta_2O_5 films compared to those of Fe-Ta_2O_5 films – see Supporting Table S1 and additional discussion in the Supporting information. Finally, the values of the electron lifetime τ and electron length diffusion L_{eff} also pinpoint that the new states introduced by the Fe impurities are effective electron trapping centers that increase the τ and reduce the L_{eff} values as directly compared to those of Ta_2O_5 films.

Based on the EIS data and the photocatalytic experiments in **Figure 5**, we could propose that both types of Fe incorporation (in the form of doping and segregated FeO_x phase), despite significantly increased absorption in the visible light range, are detrimental for the photo-reductive performance. **Scheme 2** illustrates possible charge transfer processes in the case of Fe-Ta_2O_5 NTs: in both scenarios the photoexcited electrons get trapped at the Fe impurities, loose their potential energy and become thermodynamically unable to further participate in the H^+ reduction reaction.[56]

Conclusion

In this work, we used CNTs as sacrificial templates to synthesize Ta_2O_5 nanotubes with single-crystalline walls and tunable wall thickness. We observed that the residual CNT-growth catalyst remains incorporated within the Ta_2O_5 NT walls upon oxidative CNT removal. The combined analysis by Raman spectroscopy, XPS, DRS, EDX and XRD revealed that iron incorporates both, in the form of atomic doping and segregated FeO_x nanocrystals. Further investigation with EIS shows that in both cases, the presence of iron exerts a highly detrimental effect on the performance of the NTs for photocatalytic hydrogen evolution. Importantly, this effect can be avoided by pre-annealing the CNTs at 2100 °C to prepare Fe-free-Ta_2O_5 NTs that exhibited a 40-fold higher activity compared to the Fe-containing counterpart. Consequently, the presence of residual catalyst needs to be taken with great caution when using CNT templates to design functional tubular nanostructures for many energy and environmental applications.

Methods

CNT growth and post-processing. Carbon nanotubes were grown via a continuous-flow chemical vapor deposition (CVD) process with a floating catalyst, using a two stage horizontal tube furnace (type HZS, Carbolite, UK) and a custom-built temperature-controlled syringe injection inlet. In detail, a solution of 4 wt. % ferrocene in toluene was continuously injected into a pre-heated (180 °C) inlet at a rate of 5.4 ml h^{-1} before being carried by an argon flow (400 mL min^{-1}) into the quartz reaction chamber that was heated at 760 °C. The growth time was set to 5h. After cooling the reactor, the CNTs were mechanically removed from the tube and further purified by annealing in argon at 1000 °C for 6 h (in order to remove amorphous carbon) to yield a CNT1000 sample or at 2100 °C for 6 h (in order to remove residual Fe) to yield a CNT2100 sample. Length and average outer diameter of the as-grown CNTs were approximately 200 µm and 80 nm, respectively.

Sol-gel Ta_2O_5 deposition. The CNTs (independent of the post-treatment) were hybridized with Ta_2O_5 via an aqueous sol-gel route (Scheme 1, step 1) using $Ta(OEt)_5$ as precursor, ethanol as solvent and benzyl alcohol (BA) as linking agent. In a typical experiment, 100 mg of CNTs were suspended in 70 ml ethanol, which included 50 µl deionised water and 140 µl BA and ultrasonicated for 80 minutes. 400 mg of $Ta(OEt)_5$ was dissolved in 20 ml of absolute ethanol under argon atmosphere and added drop-wise to the CNT suspension. After 24 hours of aging and stirring at room temperature, the solid material was filtered, washed with ethanol in order to removed unreacted precursor, and subjected to hydrothermal treatment at 180 °C for 24 hours. After the autoclaving, the suspension was transferred to a petri dish and dried at 60 °C to yield the CNT-Ta_2O_5 hybrid.

Ta_2O_5 NT synthesis. After drying, the CNT-Ta_2O_5 hybrids were calcined in air to remove the CNT templates (Scheme 1, steps 2 and 3). The powdered samples were heat treated in air for 5h at 780 °C (ramp 1.5 °C/min) to yield white Ta_2O_5 NT (resulting from the CNT2100 sample) and pink Fe-containing-Ta_2O_5 (resulting from the CNT1000 sample) powders (see Figure 4).

Model samples. In order to verify which of the potential impurity type – Fe doping or formation of FeO_x NPs – is responsible for the detrimental effect on photocatalytic activity, we prepared additional model samples. To prepare the Fe-doped-Ta_2O_5 NTs, we started with the pink powder of the Fe-incorporated-Ta_2O_5 NTs (sample prepared using CNT1000). It was dispersed in 5 M HCl solution and stirred for 30 h. The solution was then vacuum-filtered and thoroughly washed with water to remove any acidic residues. The resulting pink powder was then dried at 60 °C. To prepare FeO_x-containing-Ta_2O_5 NTs, we started with the white powder of the pure Ta_2O_5 NTs (sample prepared using CNT2100) and impregnated it with $Fe(NO_3)_3x9H_2O$ solution. The solution was dried at 150 °C and further calcined at as low as 250 °C for 1 h to yield additional FeO_x NPs on the Ta_2O_5 NT surface while at the same time avoiding Fe doping.

Characterization methods. Scanning electron microscopy (SEM) images were acquired using Zeiss XB 1540 EsB scanning electron microscope to obtain visual information on the long range pore order and morphology of the samples. Typically acceleration voltage of 2 kV and secondary electron detection mode were used. Transmission electron microscopy (TEM) images were obtained using FEI Tecnai F20 transmission electron microscope equipped with a field emission gun in bright field mode using 200 kV acceleration voltage. The sample was prepared from a suspension in ethanol without ultrasonication, using a copper Lacey carbon coated grids (Plano, 200 mesh). Energy dispersive X-ray spectroscopy (EDX) was performed using both SEM and TEM machines to obtain elemental maps. X-ray diffraction (XRD) was performed using Bruker D8 Advance machine with Bragg-Brentano geometry equipped with a Ni filter and a Lynxeye super speed detector using a Cu K_α irradiation with λ_1 of 1.540596 Å and λ_2 of 1.544410 Å with the ratio of 0.442227. The average crystallite size was calculated using Scherrer's equation and a shape factor of 0.9. The thermogravimetric (TGA) measurements were carried out on a TGA Q5000 (TA Instruments). The samples were filled in an Al_2O_3-crucible and stabilized isothermally at 40 °C for 1 h. A temperature ramp from 30 to 1000 °C with 5 K min^{-1} under air was applied. Raman spectra were obtained using Jobin Yvon Horiba LABRAM HR dispersive Raman spectrometer equipped with a CCD detector, a Nd:Yag-Laser (λ = 532 nm) and an Olympus BX41 optical microscope. The chemical composition of the samples was obtained with X-ray photoelectron spectroscopy (XPS) using a VG ESCALAB 250 with Al-K_{α} radiation. The optical properties of the samples were further investigated via diffuse reflectance spectroscopy (DRS) using a Jasco V-670 UV-vis photo spectrometer. An Ulbricht-sphere was used for light collection and the samples were measured with a 3 mm aperture. Electrochemical impedance spectroscopic (EIS) assays were carried out with a potentiostat/galvanostat (PGSTAT30, Autolab) equipped with a frequency response analyzer module (FRA). Multiple impedance measurements with different applied bias have been performed for each device starting at the V_{oc} and going in 0.2 V steps until the J_{sc} condition. All devices were measured in the dark and under illumination (AM 1.5 filter, 100 W/cm^2) conditions. The AC signal amplitude was set to 10 mV, modulated in a frequency range from 0.1 Hz to 100 kHz. The Nova 1.11 software was used to obtain the parameters from the equivalent circuit. With this data at hand, the charge collection efficiency yield η_{coll}, the electron lifetime τ and the effective carrier diffusion length L_{eff} were calculated by means of equations 1, 2, and 3, respectively.

$$\eta_{coll} = 1 - (R_w/R_k) \qquad (1)$$

$$\tau = 1/(2 \times \pi \times f_{max}) \qquad (2)$$

$$L_{eff} = (D_{eff} \times \tau)^{1/2} \qquad (3)$$

where R_w, R_k, f_{max}, and D_{eff} are the electron transport resistance, the charge-transfer resistance to recombination of electrons, the maximum frequency taken from the Bode phase plot, and the effective diffusion coefficient, respectively.

Photocatalytic experiments. Hydrogen evolution experiments were performed using an inner irradiation gas flow slurry type home-build reactor consisting of two cylindrical parts, each double walled, the inner cylinder completely made of quartz (HSQ300 type from Heraeus) to be transparent to the UV portion of light. A medium pressure immersion type 700 W Hg TQ 718 lamp (output power was adjusted to 500 W for all experiments) from UV Consulting company with output range of 200-600 nm was inserted in the inner cylinder. In a single experiment 50 mg of a powdered photocatalyst was dispersed in 10 vol. % MeOH-water solution by ultrasonication. Additional experiments only used 5 or 10 mg of the photocatalyst powder while keeping the rest of the experimental procedure identical. The reaction medium was then transferred to the reactor. During the experiment, the reactor was continuously purged with argon 5.8 (flow rate of 100 ml/min, controlled with a mass flow controller Q-Flow 140 Series from MCC-Instruments) to deliver the gaseous products to the online gas analyzer (X-Stream®, Emerson Process Management) equipped with thermal conductivity detector (TCD) for H_2 quantification. The temperature of the reactor was kept at 10 °C through a water cooling system from Lauda (Variocool 1200 W). In a single experiment, the suspension was first stirred for 1.5 h in dark, then illuminated for 1 h. A typical H_2 evolution profile (e.g. in Figure 5a) obtained with our flow reactor includes an "induction" period (increasing H_2 evolution rate during the first 5-10 min) that is purely related to the fact the H_2 gas first needs to fill the dead volume (e.g. reactor volume, tubing volume) to reach the detector. And visa-versa, when the illumination is stopped, the signal slowly goes down to the baseline level. Thus, for further evaluation, we only consider the steady-state rates of H_2 evolution that the catalysts reach after 1 h of the light-on cycle. In some experiments the reaction mixture was further injected with water-based H_2PtCl_6 solution to photodeposit Pt NPs (assumed loading was equal to 0.5 wt. % with respect to the photocatalyst mass) during the second light-on cycle. The H_2 evolution rates were normalized by subtracting the H_2 evolution rate measured in the blank experiment (no catalyst present in the MeOH-H_2O mixture) as a result of UV-assisted MeOH oxidation (photo-reforming).

Acknowledgements

The authors would like to acknowledge Dr. Torsten Reuter for XPS measurements, Tobias Weller for XRD analyses and Huating Hu for Raman measurements. The work was funded by the Deutsche Forschungsgesellschaft (DFG ED 221/3-1).

Supporting Information

Figure S1 (additional TEM images, TGA and Raman data on CNTs), Figure S2 and S3 (additional TEM and SEM images of the CNT-Ta_2O_5 hybrids and the resulting Ta_2O_5 NTs), Figure S4 (detailed XRD spectra), Figure S5 (additional EDX maps), Figure S6 (additional XPS and Raman data), Figure S9 (additional EIS data) as well as list of chemicals, procedure of photonic efficiency calculation (along with Figure S7) and information on EIS data analyses (along with Figure S8) are all supplied as Supporting Information.

References

(1) Fujishima, A.; Honda, K. Electrochemical Photolysis of Water at a Semiconductor Electrode. *Nature* **1972**, *238* (5358), 37–38.

(2) Maeda, K.; Teramura, K.; Lu, D.; Takata, T.; Saito, N.; Inoue, Y.; Domen, K. Photocatalyst Releasing Hydrogen from Water. *Nature* **2006**, *440* (7082), 295–295.

(3) Wang, X.; Maeda, K.; Thomas, A.; Takanabe, K.; Xin, G.; Carlsson, J. M.; Domen, K.; Antonietti, M. A Metal-Free Polymeric Photocatalyst for Hydrogen Production from Water under Visible Light. *Nat Mater* **2009**, *8* (1), 76–80.

(4) Nakata, K.; Fujishima, A. TiO2 Photocatalysis: Design and Applications. *J. Photochem. Photobiol. C Photochem. Rev.* **2012**, *13* (3), 169–189.

(5) Hisatomi, T.; Kubota, J.; Domen, K. Recent Advances in Semiconductors for Photocatalytic and Photoelectrochemical Water Splitting. *Chem. Soc. Rev.* **2014**, *43* (22), 7520–7535.

(6) Xiao, F.-X.; Miao, J.; Tao, H. B.; Hung, S.-F.; Wang, H.-Y.; Yang, H. B.; Chen, J.; Chen, R.; Liu, B. One-Dimensional Hybrid Nanostructures for Heterogeneous Photocatalysis and Photoelectrocatalysis. *Small* **2015**, *11* (18), 2115–2131.

(7) Mizuno, N.; Misono, M. Heterogeneous Catalysis. *Chem. Rev.* **1998**, *98* (1), 199–218.

(8) Rodríguez-reinoso, F. The Role of Carbon Materials in Heterogeneous Catalysis. *Carbon* **1998**, *36* (3), 159–175.

(9) Amano, F.; Nogami, K.; Tanaka, M.; Ohtani, B. Correlation between Surface Area and Photocatalytic Activity for Acetaldehyde Decomposition over Bismuth Tungstate Particles with a Hierarchical Structure. *Langmuir* **2010**, *26* (10), 7174–7180.

(10) Zou, Z.; Ye, J.; Sayama, K.; Arakawa, H. Direct Splitting of Water under Visible Light Irradiation with an Oxide Semiconductor Photocatalyst. *Nature* **2001**, *414* (6864), 625–627.

(11) Zhu, J.; Zäch, M. Nanostructured Materials for Photocatalytic Hydrogen Production. *Curr. Opin. Colloid Interface Sci.* **2009**, *14* (4), 260–269.

(12) Kasuga, T.; Hiramatsu, M.; Hoson, A.; Sekino, T.; Niihara, K. Formation of Titanium Oxide Nanotube. *Langmuir* **1998**, *14* (12), 3160–3163.

(13) Du, G. H.; Chen, Q.; Che, R. C.; Yuan, Z. Y.; Peng, L.-M. Preparation and Structure Analysis of Titanium Oxide Nanotubes. *Appl. Phys. Lett.* **2001**, *79* (22), 3702–3704.

(14) Jia, C.-J.; Sun, L.-D.; Yan, Z.-G.; You, L.-P.; Luo, F.; Han, X.-D.; Pang, Y.-C.; Zhang, Z.; Yan, C.-H. Single-Crystalline Iron Oxide Nanotubes. *Angew. Chem.* **2005**, *117* (28), 4402–4407.

(15) Krumeich, F.; Muhr, H.-J.; Niederberger, M.; Bieri, F.; Schnyder, B.; Nesper, R. Morphology and Topochemical Reactions of Novel Vanadium Oxide Nanotubes. *J. Am. Chem. Soc.* **1999**, *121* (36), 8324–8331.

(16) Mor, G. K.; Shankar, K.; Paulose, M.; Varghese, O. K.; Grimes, C. A. Enhanced Photocleavage of Water Using Titania Nanotube Arrays. *Nano Lett.* **2005**, *5* (1), 191–195.
(17) Macak, J. M.; Zlamal, M.; Krysa, J.; Schmuki, P. Self-Organized TiO2 Nanotube Layers as Highly Efficient Photocatalysts. *Small* **2007**, *3* (2), 300–304.
(18) Ghicov, A.; Schmuki, P. Self-Ordering Electrochemistry: A Review on Growth and Functionality of TiO2nanotubes and Other Self-Aligned MOx Structures. *Chem. Commun.* **2009**, No. 20, 2791–2808.
(19) Wang, G.; Wang, H.; Ling, Y.; Tang, Y.; Yang, X.; Fitzmorris, R. C.; Wang, C.; Zhang, J. Z.; Li, Y. Hydrogen-Treated TiO2 Nanowire Arrays for Photoelectrochemical Water Splitting. *Nano Lett.* **2011**, *11* (7), 3026–3033.
(20) Ajayan, P. M.; Stephan, O.; Redlich, P.; Colliex, C. Carbon Nanotubes as Removable Templates for Metal Oxide Nanocomposites and Nanostructures. *Nature* **1995**, *375* (6532), 564–567.
(21) Liang, H.-W.; Liu, S.; Yu, S.-H. Controlled Synthesis of One-Dimensional Inorganic Nanostructures Using Pre-Existing One-Dimensional Nanostructures as Templates. *Adv. Mater.* **2010**, *22*, 3925-3937.
(22) Eder, D.; Windle, A. H. Morphology Control of CNT-TiO2 Hybrid Materials and Rutile Nanotubes. *J. Mater. Chem.* **2008**, *18* (17), 2036–2043.
(23) Rao, C. N. R.; Satishkumar, B. C.; Govindaraj, A. Zirconia Nanotubes. *Chem. Commun.* **1997**, No. 16, 1581–1582.
(24) Lee, J. S.; Min, B.; Cho, K.; Kim, S.; Park, J.; Lee, Y. T.; Kim, N. S.; Lee, M. S.; Park, S. O.; Moon, J. T. Al2O3 Nanotubes and Nanorods Fabricated by Coating and Filling of Carbon Nanotubes with Atomic-Layer Deposition. *J. Cryst. Growth* **2003**, *254* (3–4), 443–448.
(25) Du, N.; Zhang, H.; Chen, B. D.; Ma, X. Y.; Liu, Z. H.; Wu, J. B.; Yang, D. R. Porous Indium Oxide Nanotubes: Layer-by-Layer Assembly on Carbon-Nanotube Templates and Application for Room-Temperature NH3 Gas Sensors. *Adv. Mater.* **2007**, *19* (12), 1641–1645.
(26) Yuan, C.; Hou, L.; Feng, Y.; Xiong, S.; Zhang, X. Sacrificial Template Synthesis of Short Mesoporous NiO Nanotubes and Their Application in Electrochemical Capacitors. *Electrochimica Acta* **2013**, *88*, 507–512.
(27) Mohammadi, M. R.; Tabei, S. A.; Nemati, A.; Eder, D.; Pradeep, T. Synthesis and Crystallization of Lead–zirconium–titanate (PZT) Nanotubes at the Low Temperature Using Carbon Nanotubes (CNTs) as Sacrificial Templates. *Adv. Powder Technol.* **2012**, *23* (5), 647–654.
(28) Sun, Z.; Yuan, H.; Liu, Z.; Han, B.; Zhang, X. A Highly Efficient Chemical Sensor Material for H2S: α-Fe2O3 Nanotubes Fabricated Using Carbon Nanotube Templates. *Adv. Mater.* **2005**, *17* (24), 2993–2997.

(29) An, G.; Zhang, Y.; Liu, Z.; Miao, Z.; Han, B.; Miao, S.; Li, J. Preparation of Porous Chromium Oxide Nanotubes Using Carbon Nanotubes as Templates and Their Application as an Ethanol Sensor. *Nanotechnology* **2008**, *19* (3), 035504 (7pp).

(30) Du, N.; Zhang, H.; Chen, B. D.; Wu, J. B.; Ma, X. Y.; Liu, Z. H.; Zhang, Y. Q.; Yang, D. R.; Huang, X. H.; Tu, J. P. Porous Co3O4 Nanotubes Derived From Co4(CO)12 Clusters on Carbon Nanotube Templates: A Highly Efficient Material For Li-Battery Applications. *Adv. Mater.* **2007**, *19* (24), 4505–4509.

(31) Kumar, M.; Ando, Y. Chemical Vapor Deposition of Carbon Nanotubes: A Review on Growth Mechanism and Mass Production. *J. Nanosci. Nanotechnol.* **2010**, *10* (6), 3739–3758.

(32) Dupuis, A.-C. The Catalyst in the CCVD of Carbon Nanotubes—a Review. *Prog. Mater. Sci.* **2005**, *50* (8), 929–961.

(33) Öncel, Ç.; Yürüm, Y. Carbon Nanotube Synthesis via the Catalytic CVD Method: A Review on the Effect of Reaction Parameters. *Fuller. Nanotub. Carbon Nanostructures* **2006**, *14* (1), 17–37.

(34) Eder, D.; Motta, M. S.; Windle, A. H. Nanoengineering with Residual Catalyst from CNT Templates. *Acta Mater.* **2010**, *58* (13), 4406–4413.

(35) Eder, D.; Motta, M.; Windle, A. H. Iron-Doped Pt-TiO2 Nanotubes for Photo-Catalytic Water Splitting. *Nanotechnology* **2009**, *20* (5), 055602 (6pp).

(36) Cherevan, A. S.; Robbins, S.; Dieterle, D.; Gebhardt, P.; Wiesner, U.; Eder, D. Ordered Gyroidal Tantalum Oxide Photocatalysts: Eliminating Diffusion Limitations and Tuning Surface Barriers. *Nanoscale* **2016**, *8* (37), 16694–16701.

(37) Cooke, D. J.; Eder, D.; Elliott, J. A. Role of Benzyl Alcohol in Controlling the Growth of TiO2 on Carbon Nanotubes. *J. Phys. Chem. C* **2010**, *114* (6), 2462–2470.

(38) Shearer, C. J.; Cherevan, A.; Eder, D. Application and Future Challenges of Functional Nanocarbon Hybrids. *Adv. Mater.* **2014**, *26* (15), 2295–2318.

(39) Chen, R. Y.; Yeun, W. Y. D. Review of the High-Temperature Oxidation of Iron and Carbon Steels in Air or Oxygen. *Oxid. Met.* **2003**, *59* (5–6), 433–468.

(40) Cherevan, A. S.; Gebhardt, P.; Shearer, C. J.; Matsukawa, M.; Domen, K.; Eder, D. Interface Engineering in Nanocarbon–Ta2O5 Hybrid Photocatalysts. *Energy Environ. Sci.* **2014**, *7* (2), 791–796.

(41) Andrews, R.; Jacques, D.; Qian, D.; Dickey, E. C. Purification and Structural Annealing of Multiwalled Carbon Nanotubes at Graphitization Temperatures. *Carbon* **2001**, *39* (11), 1681–1687.

(42) Lehovec, K. Lattice Structure of β-Ta2O5. *J. Common Met.* **1964**, *7* (6), 397–410.

(43) Audier, M.; Chenevier, B.; Roussel, H.; Lintanf Salaün, A. Second Order Incommensurate Phase Transition in 25L-Ta2O5. *J. Solid State Chem.* **2010**, *183* (9), 2068–2076.

(44) Patterson, A. L. The Scherrer Formula for X-Ray Particle Size Determination. *Phys. Rev.* **1939**, *56* (10), 978–982.

(45) Joseph, C.; Bourson, P.; Fontana, M. D. Amorphous to Crystalline Transformation in Ta2O5 Studied by Raman Spectroscopy. *J. Raman Spectrosc.* **2012**, *43* (8), 1146–1150.
(46) Choi, H. C.; Jung, Y. M.; Kim, S. B. Size Effects in the Raman Spectra of TiO2 Nanoparticles. *Vib. Spectrosc.* **2005**, *37* (1), 33–38.
(47) Balberg, I.; Pinch, H. L. The Optical Absorption of Iron Oxides. *J. Magn. Magn. Mater.* **1978**, *7* (1), 12–15.
(48) Liu, M.; Qiu, X.; Miyauchi, M.; Hashimoto, K. Energy-Level Matching of Fe(III) Ions Grafted at Surface and Doped in Bulk for Efficient Visible-Light Photocatalysts. *J. Am. Chem. Soc.* **2013**, *135* (27), 10064–10072.
(49) Jing, D.; Guo, L. Hydrogen Production over Fe-Doped Tantalum Oxide from an Aqueous Methanol Solution under the Light Irradiation. *J. Phys. Chem. Solids* **2007**, *68* (12), 2363–2369.
(50) Rehman, S.; Ullah, R.; Butt, A. M.; Gohar, N. D. Strategies of Making TiO2 and ZnO Visible Light Active. *J. Hazard. Mater.* **2009**, *170* (2), 560–569.
(51) Pelaez, M.; Nolan, N. T.; Pillai, S. C.; Seery, M. K.; Falaras, P.; Kontos, A. G.; Dunlop, P. S. M.; Hamilton, J. W. J.; Byrne, J. A.; O'Shea, K.; Entezari, M. H.; Dionysiou, D. D. A Review on the Visible Light Active Titanium Dioxide Photocatalysts for Environmental Applications. *Appl. Catal. B Environ.* **2012**, *125* (Supplement C), 331–349.
(52) Marschall, R.; Wang, L. Non-Metal Doping of Transition Metal Oxides for Visible-Light Photocatalysis. *Catal. Today* **2014**, *225*, 111–135.
(53) Bloh, J. Z.; Dillert, R.; Bahnemann, D. W. Zinc Oxide Photocatalysis: Influence of Iron and Titanium Doping and Origin of the Optimal Doping Ratio. *ChemCatChem* **2013**, *5* (3), 774–778.
(54) Piskunov, S.; Lisovski, O.; Begens, J.; Bocharov, D.; Zhukovskii, Y. F.; Wessel, M.; Spohr, E. C-, N-, S-, and Fe-Doped TiO2 and SrTiO3 Nanotubes for Visible-Light-Driven Photocatalytic Water Splitting: Prediction from First Principles. *J. Phys. Chem. C* **2015**, *119* (32), 18686–18696.
(55) Wieczorek-Ciurowa, K.; Kozak, A. J. The Thermal Decomposition of Fe(NO<Subscript>3</Subscript>)<Subscript>3·</Subscript>9H<Subscript>2</Subscript>O. *J. Therm. Anal. Calorim.* **1999**, *58* (3), 647–651.
(56) George, S.; Pokhrel, S.; Ji, Z.; Henderson, B. L.; Xia, T.; Li, L.; Zink, J. I.; Nel, A. E.; Mädler, L. Role of Fe Doping in Tuning the Band Gap of TiO2 for the Photo-Oxidation-Induced Cytotoxicity Paradigm. *J. Am. Chem. Soc.* **2011**, *133* (29), 11270–11278.